

Simulating the Impact of X-ray Heating during the Cosmic Dawn

Hannah E. Ross,^{1,2} * Keri L. Dixon¹, Ilian T. Iliev¹ and Garrelt Mellema²

¹ *Astronomy Centre, Department of Physics & Astronomy, Pevensey II Building, University of Sussex, Falmer, Brighton, BN1 9QH, United Kingdom*

² *Department of Astronomy & Oskar Klein Centre, AlbaNova, Stockholm University, SE-106 91 Stockholm, Sweden*

11 April 2022

ABSTRACT

Upcoming observations of the 21-cm signal from the Epoch of Reionization will soon provide us with the first direct detection of this era. This signal is influenced by many astrophysical effects, including long range X-ray heating of the intergalactic gas. During the preceding Cosmic Dawn era the impact of this heating on the 21-cm signal is particularly prominent, especially before spin temperature saturation. We present the largest-volume ($244 h^{-1} \text{Mpc} = 349 \text{ Mpc}$ comoving) full numerical radiative transfer simulations to date of this epoch, including the effects of helium and multi-frequency heating, both with and without X-ray sources. We show that X-ray sources can contribute significantly to early heating of the neutral intergalactic medium and, hence, to the corresponding 21-cm signal. The inclusion of hard, energetic radiation yields an earlier, extended transition from absorption to emission compared to the stellar-only case. The presence of X-ray sources decreases the absolute value of the mean 21-cm differential brightness temperature. These hard sources also significantly increase the 21-cm fluctuations compared the common assumption of temperature saturation. The power spectrum is initially boosted on large scales before decreasing on all scales. Compared to the case of the cold, unheated intergalactic medium, the signal has lower rms fluctuations and increased non-Gaussianity, as measured by the skewness and kurtosis of the 21-cm probability distribution functions. Images of the 21-cm signal with resolutions around 11 arcmin still show fluctuations well above the expected noise for deep integrations with the SKA1-Low, indicating that direct imaging of the X-ray heating epoch could be feasible.

Key words: cosmology: theory — radiative transfer — reionization — intergalactic medium — large-scale structure of universe — galaxies: formation

1 INTRODUCTION

The Epoch of Reionization (EoR), a major global phase transition in which the neutral hydrogen in the Universe transitioned from almost neutral to largely ionized, remains one of the cosmological eras least constrained by observations. Although no direct measurements of this transition currently exist, multiple observations indicate reionization is completed by $z \approx 5.7$ and possibly earlier. These observations include high-redshift quasar spectra (e.g. Fan et al. 2006; McGreer et al. 2015), the decrease in the fraction of Lyman α (Ly α) emitting galaxies (e.g. Stark et al. 2011; Schenker et al. 2012; Pentericci et al. 2014; Tilvi et al. 2014), and measurements of the temperature of the intergalactic medium (IGM; e.g. Theuns et al. 2002; Raskutti et al. 2012; Bolton et al. 2012). The start of substantial reionization is constrained by the Thomson optical depth measured from the anisotropies and polarisation of the Cosmic Microwave Background, CMB, (e.g. Komatsu et al. 2011; Planck Collaboration et al. 2015, 2016). Planck Collaboration et al.

(2016) find that the Universe was less than 10 per cent ionized at redshift 10, the average redshift at which reionization would have taken place if it had been an instantaneous process to be in the range $7.8 \leq z \leq 8.8$, and an upper limit for the duration of the process is $\Delta z < 2.8$.

At high redshifts, 21-cm radiation from hydrogen atoms in the IGM contains a treasure trove of information about the physical conditions both during the EoR and the preceding epochs. In particular, the 21-cm signal probes the *Dark Ages*, the epoch after recombination during which the formation of baryonic large scale structure began and the *Cosmic Dawn*, the period of preheating from the first ionizing sources before reionization was significantly underway. Several experiments are attempting to measure the 21-cm signal from the EoR using low-frequency radio interferometry.

* email: H.Ross@sussex.ac.uk

These include GMRT¹, LOFAR², MWA³, and PAPER⁴ and the future HERA⁵ and SKA⁶.

The main sources powering reionization are likely early galaxies, with Population III (Pop. III; metal-free) and Population II (Pop. II; metal-enriched) stars providing the bulk of ionizing photons. However, sources of higher energy X-ray photons may also be present, contributing non-trivially to the photon budget. Although their abundance is uncertain, X-ray binaries likely exist throughout reionization (Glover & Brand 2003). Other hard radiation sources, such as QSOs and supernovae, may also have contributed. Very little is known about these objects in terms of their abundances, clustering, evolution and spectra especially at these high redshifts.

The high-energy photons from these hard radiation sources have a much smaller cross section for interaction with atoms and, hence, far longer mean free path than lower energy ionizing photons. Therefore, these photons are able to penetrate significantly further into the neutral IGM. While not sufficiently numerous to contribute significantly to the ionization of the IGM (although recently there has been some debate about the level of contribution of quasars, (e.g. Khaire et al. 2016)), their high energies result in a non-trivial amount of heating. Along with variations in the early Ly α background, variations in the temperature of the neutral IGM caused by this non-uniform heating constitute an important source of 21-cm fluctuations before large-scale reionization patchiness develops (see e.g. Pritchard & Loeb 2012, for a detailed discussion).

Once a sufficient Ly α background due to stellar radiation has been established in the IGM, the spin temperature of neutral hydrogen will be coupled to the kinetic temperature due to the Wouthuysen-Field (WF) effect. The 21-cm signal is then expected to appear initially in absorption against the CMB, as the CMB temperature (T_{CMB}) is greater than the spin temperature of the gas. Once heating by the first sources has heated the IGM and brought the spin temperature above T_{CMB} , the signal transitions into emission (see Section 3.1 for more details). The timing and duration of this transition are highly sensitive to the type of sources present, as they determine the quantity and morphology of the heating of the IGM (e.g. Pritchard & Furlanetto 2007; Baek et al. 2010; Mesinger et al. 2013; Fialkov et al. 2014; Pacucci et al. 2014; Ahn et al. 2015b).

Considerable theoretical work regarding the impact of X-ray radiation on the thermal history of reionization and the future observational signatures exists. Attempts have been made to understand the process analytically (e.g. Glover & Brand 2003; Furlanetto et al. 2004), semi-numerically (see e.g. Santos et al. 2010; Mesinger et al. 2013; Fialkov et al. 2014; Kneivitt et al. 2014), and numerically (e.g. Baek et al. 2010; Xu et al. 2014; Ahn et al. 2015b). However, due to the computationally challenging, multi-scale nature of the problem, numerical simulations have not yet been run over a sufficiently large volume – a few hundred comoving Mpc per side – to properly account for the patchiness of reionization (Iliev et al. 2014), while at the same time resolving the ionizing sources.

In this paper, we present the first full numerical simulation of reionization including X-ray sources and multi-frequency heating over hundreds of Mpc scales. Using multi-frequency radiative transfer (RT) modelling, we track the morphology of the heating

and evolution of ionized regions using density perturbations and haloes obtained from a high-resolution, N -body simulation. The size of our simulations ($244 h^{-1}$ Mpc = 349 Mpc comoving on a side) is sufficiently large to capture the large-scale patchiness of reionization and to make statistically meaningful predictions for future 21-cm observations. We compare two source models, one with and one without X-ray sources, that otherwise use the same underlying cosmic structures. We also test the limits of validity of the common assumption that for late times the IGM temperature is much greater than the spin temperature.

The outline of the paper is as follows. In Section 2, we present our simulations and methodology. In Section 3, we describe in detail the theory behind our generation of the 21-cm signatures. Section 4 contains our results, which include the reionization and temperature history and morphology. We also present our 21-cm maps and various statistics of the 21-cm signal. We then conclude in Section 5.

The cosmological parameters we use throughout this work are $(\Omega_{\Lambda}, \Omega_{\text{M}}, \Omega_{\text{b}}, n, \sigma_8, h) = (0.73, 0.27, 0.044, 0.96, 0.8, 0.7)$; where the notation has the usual meaning and $h = H_0/(100 \text{ km s}^{-1} \text{ Mpc}^{-1})$. These values are consistent with the latest results from WMAP (Komatsu et al. 2011) and Planck combined with all other available constraints (Planck Collaboration et al. 2015, 2016).

2 THE SIMULATIONS

In this section, we present an overview of the methods used in our simulations. We start with a high resolution N -body simulation, which provides the underlying density fields and dark matter halo catalogues. We then apply ray-tracing RT to a density field that is smoothed to a lower resolution to speed up the calculations. The sources of ionizing and X-ray radiation are associated with the dark matter haloes. Below we describe these steps in more detail.

2.1 N -BODY SIMULATIONS

The cosmic structures underlying our simulations are based on a high-resolution N -body simulation using the CUBEP³M code (Harnois-Déraps et al. 2013). A 2-level particle-mesh is used to calculate the long-range gravitational forces, kernel-matched to local, direct and exact particle-particle interactions. The maximum distance between particles over which the direct force is calculated is a parameter for the code and is currently set to 4 times the mean interparticle spacing, which was found to give the optimum trade off between accuracy and computational expense. Our N -body simulation follows 4000^3 particles in a $244 h^{-1} \text{ Mpc} = 349 \text{ Mpc}$ per side volume, and the force smoothing length is set to 1/20th of the mean interparticle spacing (this N -body simulation was previously presented in Dixon et al. (2016) and completed under the Partnership for Advanced Computing in Europe, PRACE, Tier-0 project called PRACE4LOFAR). This particle number is chosen to ensure reliable halo identification down to $10^9 M_{\odot}$ (with a minimum of 40 particles).

The linear power spectrum of the initial density fluctuations was calculated with the code CAMB (Lewis et al. 2000). Initial conditions were generated using the Zel'dovich approximation at sufficiently high redshifts (initial redshift $z_i = 150$) to ensure against numerical artefacts (Crocce et al. 2006).

¹ <http://gmrt.ncra.tifr.res.in/>

² <http://www.lofar.org/>

³ <http://www.mwatelescope.org/>

⁴ <http://eor.berkeley.edu/>

⁵ <http://reionization.org/>

⁶ <https://www.skatelescope.org/>

2.2 SOURCES

Sources are assumed to live within dark matter haloes, which were found using the spherical overdensity algorithm with an overdensity parameter of 178 with respect to the mean density. As mentioned previously, the CubeP³M simulation directly resolves haloes down to a mass of $10^9 M_\odot$. We use a sub-grid model (Ahn et al. 2015a) calibrated to very high resolution simulations to add the haloes down to $10^8 M_\odot$, the rough limit for the atomic line cooling of primordial gas to be efficient.

For a source with halo mass M and lifetime t_s , we assign a stellar ionizing photon emissivity according to

$$\dot{N}_\gamma = g_\gamma \frac{M \Omega_b}{\mu m_p (10 \text{ Myr}) \Omega_0}, \quad (1)$$

where the proportionality coefficient g_γ reflects the ionizing photon production efficiency of the stars per stellar atom, N_i , the star formation efficiency, f_* , and the escape fraction, f_{esc} :

$$g_\gamma = f_* f_{\text{esc}} N_i \left(\frac{10 \text{ Myr}}{t_s} \right). \quad (2)$$

(Haiman & Holder 2003; Iliev et al. 2012).

Sources hosted by high mass haloes (above $10^9 M_\odot$) have efficiency $g_\gamma = 1.7$ and are assumed not to be affected by radiative feedback, as their halo mass is above the Jeans mass for ionized, $\sim 10^4 \text{ K}$ gas. Low-mass haloes (between $10^8 M_\odot$ and $10^9 M_\odot$) have a higher efficiency factor $g_\gamma = 7.1$ reflecting the likely presence of more efficient Pop. III stars or higher escape fractions (Iliev et al. 2007). The low mass sources are susceptible to suppression from photoionization heating. In this work, we assume that all low-mass sources residing in ionized cells (with an ionized fraction greater than 90 per cent) are fully suppressed, i.e. they produce no ionizing photons (Iliev et al. 2007; Dixon et al. 2016). The source model for the stellar radiation is identical to the one in simulation LB2 in Dixon et al. (2016) and thus uses the aggressive suppression model ‘S’ defined there. However, the details of this suppression are not very significant here, since we focus on the very early stages of reionization before significant ionization patchiness develops. The stellar sources are assigned a blackbody spectrum with an effective temperature of $T_{\text{eff}} = 5 \times 10^4 \text{ K}$.

The X-ray sources also are assumed to reside in dark matter haloes. They are assigned a power-law spectrum with an index of -1.5 in luminosity, extending from 272.08 eV to 100 times the third ionization of helium (5441.60 eV). Photons with frequencies below the minimum frequency are assumed to be obscured as suggested by observational works (e.g. Lutovinov et al. 2005). This value for minimum frequency is consistent with the optical depth from high redshift gamma bursts (Totani et al. 2006; Greiner et al. 2009) and is also taken to be the minimum unobscured frequency in Mesinger et al. (2013).

The X-ray luminosity is also set to be proportional to the halo mass with the same efficiency factor for all active sources. Low mass haloes that are suppressed are assumed not to produce X-ray radiation. The efficiency is parametrised as follows:

$$g_x = N_x f_* \left(\frac{10 \text{ Myr}}{t_s} \right) \quad (3)$$

where f_* is the fraction of baryons that become stars and N_x is the number of X-ray photons per stellar baryon. A value of $N_x = 0.2$ is roughly consistent with measurements between 0.5–8 keV for x-ray binaries in local, star-bursting galaxies (Mineo et al. 2012) although the uncertainty on that number is a factor 2 to 3 (see the discussion in Mesinger et al. 2013). We take $g_x = 8.6 \times 10^{-2}$

which implies a star formation efficiency $f_* \approx 0.4$ if $N_x = 0.2$ and correspondingly lower if N_x would be higher. Our X-ray luminosities are therefore somewhat higher than in the local Universe but not by much.

2.3 RT SIMULATIONS

The RT is based on short characteristics ray-tracing for ionizing radiation (e.g. Raga et al. 1999) and non-equilibrium photoionization chemistry of hydrogen and helium, using the code C²-RAY, Conservative, Causal **Ray** tracing (Mellema et al. 2006). C²-RAY is explicitly photon-conserving in both space and time due to the finite-volume approach taken when calculating the photoionization rates and the time-averaged optical depths used. This quality enables time steps much longer than the ionization time scale, which results in the method being orders of magnitude faster than other approaches. However, we note that following the gas heating with high precision could impose some additional constraints on the time stepping, resulting in smaller timesteps as discussed in Lee et al. (2016).

The basic RT method was further developed in order to accommodate multi-frequency RT (Friedrich et al. 2012). The effects of helium and detailed heating are included in order to correctly model the effects of hard radiation. The developments include full on-the-spot approximation, multi-frequency photoionization, secondary ionizations, and heating. Frequency bin-integrated rates are used for the photoionization and photoionization heating rates. These are pre-calculated and stored in look up tables as functions of the optical depths at the ionization thresholds. C²-RAY has been tested extensively against existing exact solutions (Mellema et al. 2006), numerous other numerical codes within code comparison projects (Iliev et al. 2006, 2010), and against CLOUDY (Friedrich et al. 2012).

In this work, we present two simulations: one in which the haloes contain both X-ray & stellar sources, and one which only considers stellar sources. The stellar component and underlying cosmic structures are identical in both simulations. The density is smoothed onto an RT grid of size 250^3 . These simulations were performed under the PRACE Tier-0 projects PRACE4LOFAR and Multi-scale Reionization.

3 THE 21-CM SIGNAL

In this section, we discuss the method of extracting the 21-cm signal from our simulation outputs.

3.1 THE DIFFERENTIAL BRIGHTNESS TEMPERATURE

Observations aim to detect the redshifted 21-cm signal caused by the hyperfine transition from the triplet to singlet ground state of the neutral hydrogen present during reionization. This signal is dictated by the density of neutral hydrogen atoms and the ratio of hydrogen atoms in the triplet and singlet states, quantified by the spin temperature (T_S):

$$\frac{N_1}{N_0} = \frac{g_1}{g_0} \exp \left(-\frac{T_*}{T_S} \right), \quad (4)$$

where $T_* = \frac{h\nu_{10}}{k} = 0.0681 \text{ K}$ is the temperature corresponding to of the 21-cm transition energy and $g_{1,0}$ are the statistical weights of the triplet and singlet states, respectively.

For the 21-cm signal to be visible against the CMB, the spin temperature needs to decouple from it, since the two start in equilibrium at high redshift. There are two mechanisms that can do this (Field 1958). Firstly, collisions with other atoms and free electrons do so by exciting electrons from the singlet to triplet state. This mechanism is only effective for sufficiently dense gas, i.e. in very dense filaments and haloes or at very high redshifts. Secondly, the electrons can be excited to the triplet state through the Wouthuysen-Field effect when absorbing a Ly α photon. The spin temperature can then be expressed as follows (Field 1958):

$$T_S = \frac{T_{\text{CMB}} + x_\alpha T_c + x_c T_k}{1 + x_\alpha + x_c}, \quad (5)$$

where T_c is the Ly α colour temperature, x_α is the Ly α coupling constant, T_k is the gas kinetic temperature, and x_c is the collisional coupling constant. Throughout this paper, we assume that Ly α radiation is in the Wouthuysen-Field effect saturated regime (in which case $x_\alpha \gg x_c$), and the colour temperature is equal to the kinetic temperature ($T_c = T_k$); and, hence, $T_S = T_k$. Since early sources produce copious amounts of soft-UV photons, this approximation tends to hold throughout most of the evolution, except for the earliest times (e.g. Ciardi & Madau 2003).

The 21-cm signal itself is usually defined in terms of the differential brightness temperature with respect to the CMB:

$$\delta T_b = \left(1 - \frac{T_{\text{CMB}}}{T_S}\right) \frac{3\lambda_0^3 A_{10} T_\star n_{\text{HI}}(z)}{32\pi T_S H(z)(1+z)}, \quad (6)$$

where $\lambda_0 = 21.1$ cm is the line rest-frame wavelength, $A_{10} = 2.85 \times 10^{-15} \text{ s}^{-1}$ is the Einstein-A coefficient for spontaneous emission from the triplet to singlet state, and n_{HI} is the density of neutral hydrogen. Thus, δT_b could be seen either in absorption or emission, depending on the spin temperature relative to the CMB. We are particularly interested in the timing and character of the transition between absorption and emission. Predicted 21-cm maps (smoothed to the resolution of observations) and their statistical measures will be the only way to connect theories of galaxy formation to future observations of 21-cm radiation.

When calculating the 21-cm signal, many studies assume the IGM gas to have reached temperature saturation, i.e. to be heated to temperatures well above the CMB, $T_K \gg T_{\text{CMB}}$. We refer to this as the high-temperature limit (high- T_K limit). While this approximation may hold during the later stages of reionization, it certainly breaks down at early times. Where appropriate, we show the high- T_K limit results for reference.

3.2 TEMPERATURE OF THE NEUTRAL IGM IN PARTIALLY IONISED REGIONS

Very small H II regions can have sizes smaller than our cell resolution and, therefore, be unresolved in our simulations. The cells containing such ionized regions will appear partially ionized in the simulation, with a temperature that is averaged between the hot, ionized gas phase and the colder, neutral one. When calculating the differential brightness temperature based on these averaged values, we find an average signal in emission. In reality, the average signal for that region should be in absorption. We therefore obtain the temperature of the neutral phase, T_{HI} , as follows:

$$T_{\text{HI}} = \frac{T_{\text{code}} - x T_{\text{HII}}}{1 - x}, \quad (7)$$

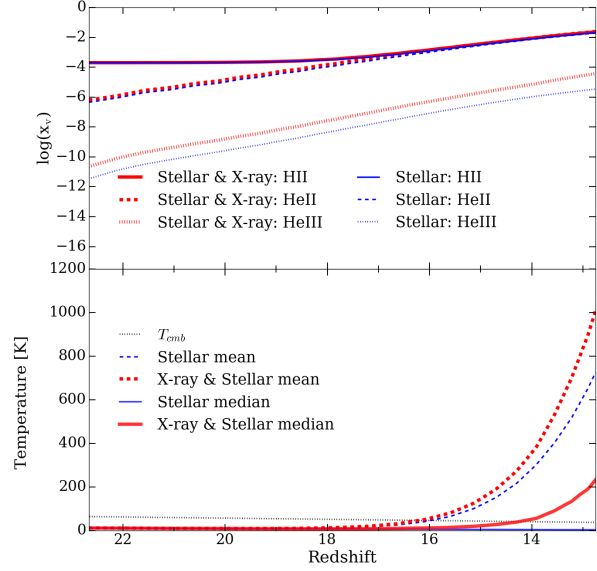


Figure 1. (top) The mean ionized fraction by volume of each species: HII - solid lines, HeII - dashed lines and HeIII - dotted lines. (bottom) The volume-weighted mean temperature - dashed lines, median temperature - solid lines and T_{CMB} - dotted line. In both plots the X-ray & stellar case is shown in red and the stellar only case is shown in blue.

where T_{code} is the cell temperature found in the simulation, T_{HII} is the mean temperature of the ionized phase (taken here to be $2.0 \times 10^4 \text{ K}$), and x is the ionized fraction of hydrogen in that cell.

4 RESULTS

4.1 REIONIZATION AND THERMAL HISTORIES

The 21-cm signal is affected by the thermal and ionization histories of the IGM. In the upper panel of Fig. 1, we show the mean volume-weighted ionized fraction evolution for three species present in our simulations, H II (solid lines), He II (dashed lines), and He III (dotted lines). The ionization of H I and He I is largely driven by the hard UV photons of stars, which are much more abundant than X-ray photons. The effect of the latter is largely limited to increasing the He III abundance by about an order of magnitude (while remaining low) due to their high energies per photon.

In the lower panel, the median (solid lines) and volume-weighted mean (dashed lines) temperatures are shown. The mean temperatures are increased modestly, surpassing T_{CMB} marginally earlier than in the stellar-only case, with both occurring around $z \sim 16$. The differences between the two cases (with and without X-rays) grow at later times, rising above 50 per cent for $z < 13$. More relevant to the 21-cm signal is the temperature of the neutral phase, which is more closely tracked by the median IGM temperature, since the mean is skewed towards higher values by the hot, ionized regions. In the presence of X-rays, the median surpasses T_{CMB} just before $z = 14$; while in their absence, this never occurs, with the neutral IGM remaining cold.

⁷ This temperature is obtained from smaller high-resolution boxes. We find that the results are insensitive to the precise value used.

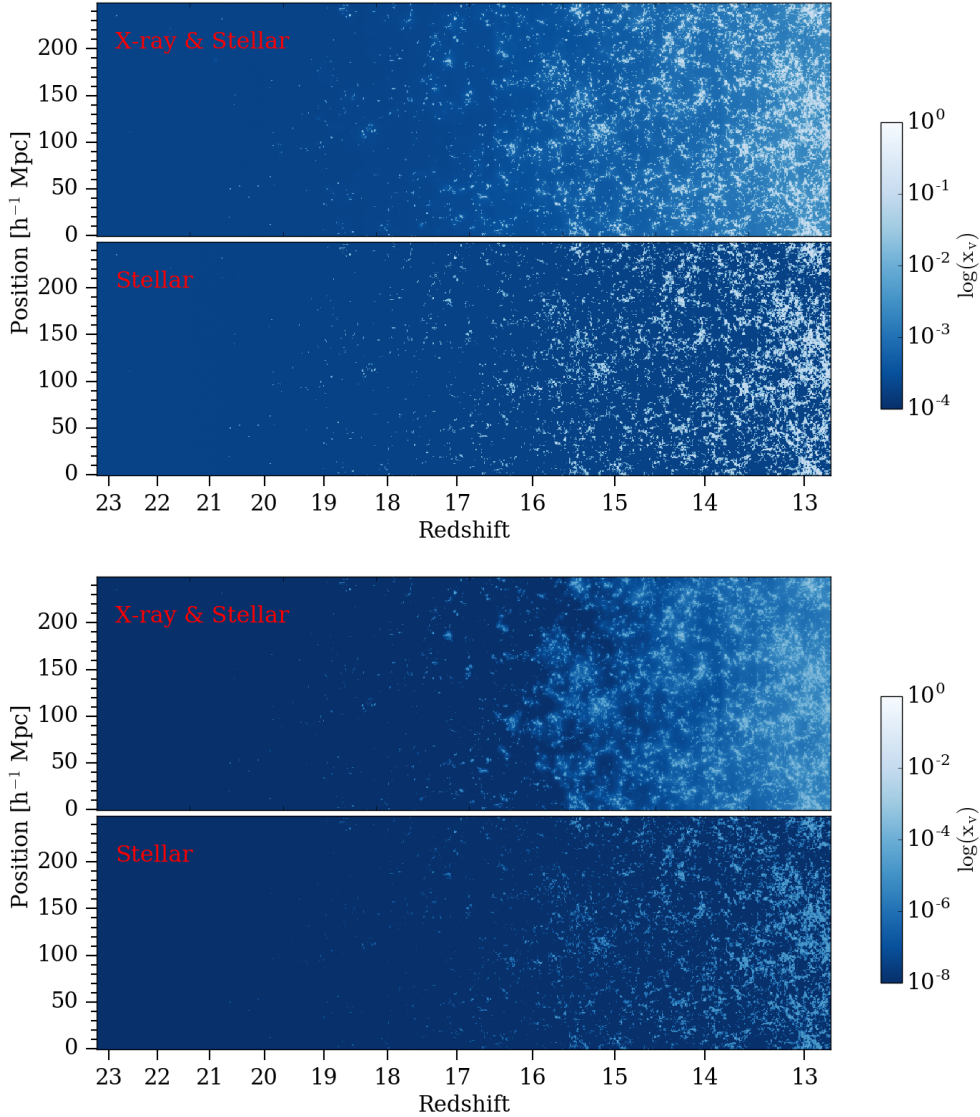


Figure 3. The position-redshift lightcone images of the ionized volume fraction of hydrogen (top two panels) and He III (bottom two panels). Shown are the X-ray & stellar case (top panel in each pair), and the stellar-only case (lower panel in each pair).

The only previous full numerical simulations which take into account X-ray sources are from Baek et al. (2010)⁸. However, the mass resolution of these simulations is approximately 600 times lower than ours, and the volume is 15 times smaller. As a consequence, their first sources of any type of radiation appear around $z \approx 14$, approximately when the neutral IGM in our simulation has already been globally heated to well above the CMB temperature. In other words, their simulations describe a scenario in which X-ray sources appear very late, are relatively rare and bright, and are coincident with substantial stellar emission. This situation is very different from our case in which the first X-ray sources appear at $z \approx 23$ and large numbers of relatively faint sources heat the neutral IGM well before any substantial reionization. We will,

therefore, not further compare the details of our results to those of Baek et al. (2010).

More detailed information about the temperature distributions is obtained from the corresponding PDFs, shown in Fig. 2. These PDFs were generated from the coeval simulation cubes using 100 bins and normalised to have a total area of one. The stellar-only distributions are clearly bimodal, with a few hot, partially ionized regions and the majority of cells remaining very cold. This behaviour is expected, given the very short mean free path of the ionizing photons in this case, which yields sharp ionization fronts. In contrast, when X-rays are present, their long mean free paths lead to gas heating spreading quickly and widely, with all cells being affected. The distribution is strongly peaked, relatively wide, and gradually moves towards higher temperatures, with typical values above 100 K by $z = 13.2$. Our thermal history is similar to that of Case A (Pop. II stars) in Pritchard & Furlanetto (2007) and case “ $\log \zeta_X = 55$ ” in Watkinson & Pritchard (2015). They do not provide temperature PDFs or median values.

⁸ There are also the simulations in Xu et al. (2014) and Ahn et al. (2015b). These studies focused a single X-ray source in a zoomed region of a cosmological volume, so are not directly comparable to our results here.

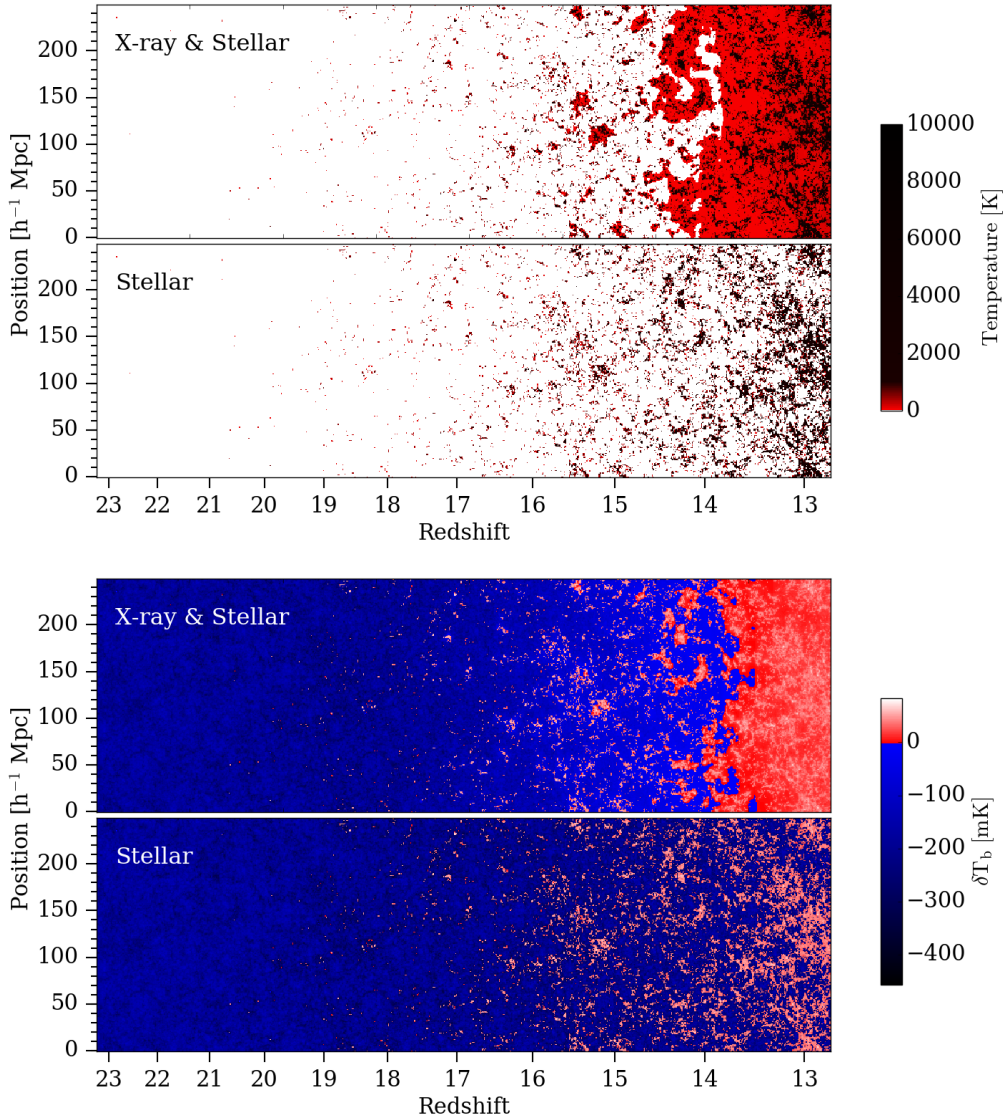


Figure 4. The position-redshift lightcone images of the IGM gas temperature (top two panels) and 21-cm differential brightness temperature (bottom two panels). Shown are the X-ray & stellar case (top panel in each pair), and the stellar-only case (lower panel in each pair).

The lightcones (spatial-redshift/frequency slices) provide a more visual representation of the quantities discussed above, including spatial variations and evolution over time (Fig. 3). These lightcones are constructed by taking a cross section of the simulation volume along the line of sight and continually interpolating in time the relevant quantity using the spatial periodicity of our cosmological volume.

In Fig. 3 (top panels), we show the hydrogen ionization lightcone. As expected based on the very similar mean ionization fractions in the two simulations, the morphology of hydrogen ionization is broadly similar. However, the hard photons, which penetrate deep into the neutral regions produce a low-level, but widespread ionization of the IGM and ‘fuzzier’, less clearly defined H II regions when X-ray sources are present. Given their similar ionization potentials, the first ionization of helium (not shown here) closely follows the one for hydrogen. Alternatively, the second helium ionization potential is sufficiently higher to result in significant differences between models (Fig. 3, bottom panels). The

50,000 K blackbody stellar spectra produce very few photons able to fully ionize a helium atom, thus any He III produced is concentrated in the immediate surroundings of the ionizing sources. However, the X-rays are very efficient in fully ionizing helium, producing widespread ionization (albeit still at a relatively low level). This ionization is also quite patchy on large scales, especially early on. The exact morphology depends on the spectra, abundance, and clustering of the X-ray sources.

The lightcones in Fig. 4 (top panels) show the spatial geometry and evolution of the IGM heating. The soft, stellar radiation in both models ionize and heat the immediate environments of the sources to $T \sim 10^4$ K, seen as dark regions, with the majority of the IGM remaining completely cold. The X-ray radiation propagates much further, starting to heat the gas throughout. Large, considerably hotter regions (red in the image) develop, quickly reaching tens of Mpc across before $z \sim 15$. These regions gradually expand and merge, resulting in thorough heating to hundreds of degrees by $z \sim 14$; though, large cold regions still remain present down to

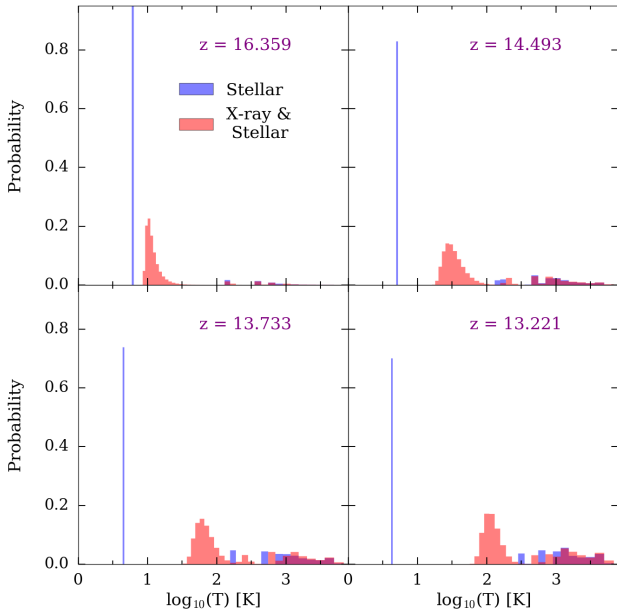


Figure 2. Histograms of the temperature at the full simulation resolution for X-rays & stellar (red) and stellar-only (blue) spectra for several illustrative redshifts.

$z \sim 13.5$. At early times, the heating increases the inhomogeneity when X-rays are present, but the temperature distribution eventually becomes more homogeneous at later times.

4.2 21-CM DIFFERENTIAL BRIGHTNESS TEMPERATURE

We are primarily interested in the directly observable quantity of this epoch, the differential brightness temperature δT_b . As discussed in Section 3, δT_b depends on the density, ionization, and temperature fields. In Fig. 4 (bottom panels), we show the δT_b lightcones corresponding to the same cross section through the position-redshift image cube as in Fig. 3 and Fig. 4 (top panels). The morphology of the δT_b fluctuations is closely related to that of the heating, demonstrating the importance of temperature variations, especially during the early stages of the EoR. Long-range X-ray heating produces a gradual, extended transition from absorption into emission. Large-scale fluctuations are significant throughout, and the first emission regions appear along with the first sources at $z = 21$. These initial bubbles grow quickly, with some reaching tens of Mpc in size by $z \sim 15.5$. Only after $z \sim 13.5$ all regions which show 21cm absorption have disappeared.

Comparing to the results of Mesinger et al. (2013), the results of our simulation appear to be closest to their case with X-ray efficiency $f_x = 1$. They also find an extended transition from absorption to emission starting at $z \sim 20$, which completes around $z \sim 14$. However, by that time, the hydrogen ionization fraction is around 10 per cent, which is substantially higher than our case. The majority of the difference is likely due to the fact that their sources are more efficient, as indicated by a completion of reionization by $z_{\text{reion}} \sim 8$ in their case versus $z_{\text{reion}} < 6.5$ for us (Dixon et al. 2016).

In the stellar-only case, the signal remains in absorption

throughout the simulation as there are no photons with long enough mean free paths to penetrate and heat the neutral IGM, which then just cools adiabatically as the universe expands⁹. The only 21-cm emitting regions in the stellar only case are the ionized patches, and there, the neutral gas fraction is very low.

In Fig. 5, we show the power spectra of δT_b at several key redshifts. During the early evolution (shown is $z = 18.186$), only a modest amount of heating of the IGM has yet occurred in either model. Thus, the large-scale 21-cm fluctuations are dominated by the density variations, which are the same in the two cases, yielding almost identical results. The high- T_K limit results in significantly lower fluctuations, reflecting the lower average δT_b in the emission regime compared to absorption or mixed regime. Compared to the high- T_K limit, there is additional small-scale power in both cases, which is due to the increased contrast between the small, hot ionized regions and the mean, cold IGM. As the evolution progresses and with X-ray sources contributing to the long-range heating, the 21-cm power is significantly boosted on large scales and a well-defined, if broad, peak develops at scale of $\sim 30 h^{-1} \text{Mpc}$ ($z = 15 - 16$). On the other hand, the small-scale power decreases due to the stronger heating in the vicinity of sources, which brings the temperature contrast with the CMB down and closer to the high- T_K limit. The overall fluctuations peak at $\sim 25 \text{ mK}$ around $z \sim 15.5$ in the X-rays & stellar model. This X-ray heating peak is also present in more approximate models results (e.g. Pritchard & Furlanetto 2007), at roughly similar scales ($k \sim 0.2 h \text{Mpc}^{-1}$), but reaching a lower peak value of order 20 mK. Pacucci et al. (2014) find a power spectra peak at a similar scale and at similar redshift ($z \sim 15 - 16$), but their value is noticeably lower, at $\Delta_{21\text{cm}} \sim 15 \text{ mK}$.

Over time, as emission patches develop and the overall IGM is gradually heated ($z = 12 - 14$) the power spectra slowly approach the high- T_K limit, but never quite reach it even by the end of our simulation. At that point ($z = 12.7$), the IGM has been heated well above T_{CMB} throughout and, thus, in 21-cm emission everywhere. However, the neutral IGM temperatures remain at only a few hundred degrees (and are still considerably spatially inhomogeneous), thus are not yet fully in the high- T_K limit where the differential brightness temperature becomes independent of the actual gas temperature value.

The evolution is quite different in the stellar-only case. The power spectra are nearly a power law at all times, with an evolving slope and amplitude. For $z \gtrsim 16$, the fluctuations on large scales decrease with time, while those on small scales do not change significantly. This difference is driven by the creation of relatively small ionized and heated regions, while the IGM largely remains cold. As the mean neutral mass slightly decreases and the neutral IGM cools down due to the Hubble expansion, the fluctuations remain roughly constant over time and on all scales and the power spectra attain a steep, power-law-like shape. Later on ($z \lesssim 14$), larger H II regions develop, with a spatial distribution modulated by the large-scale density fluctuations. The contrast between the ionized regions and the large, cold neutral regions boosts the fluctuations on all scales. Overall, the power in the stellar-only case remains far higher at late times than when X-ray heating is present, since the latter approaches and then surpasses T_{CMB} while the IGM in the former case remains very cold.

⁹ There is also some Compton heating due to CMB scattering, which we do include in our simulation. This heating is inefficient at this point due to the low density of the IGM.

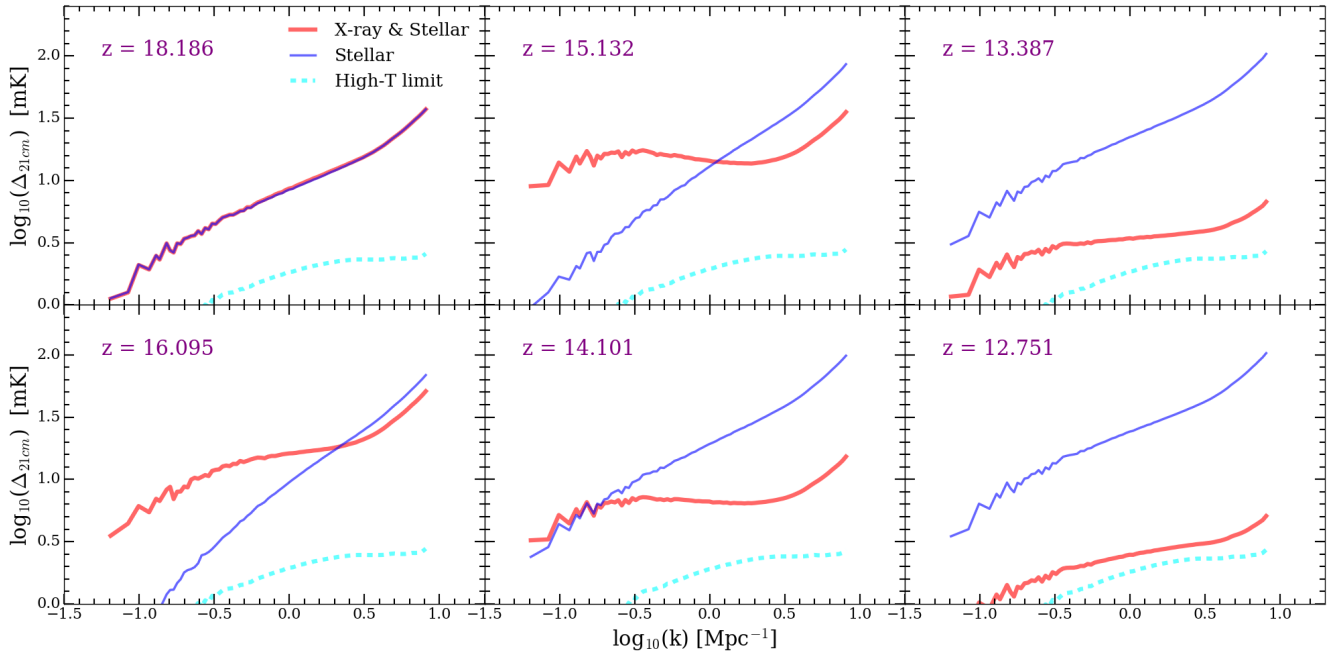


Figure 5. The 21-cm power spectra from our simulations at several key stages of the evolution with the high- T_K limit results for reference. The high- T_K limit is shown in yellow and as before the results from the X-ray & stellar case are shown in red and the stellar only case in blue.

The evolution of several particular k -modes ($k = 0.1, 0.5$, and 1 Mpc^{-1}) is shown in Fig. 6. With X-rays present, the heating peak is seen at all scales considered here, but over time it gradually moves towards larger scales, from $z \sim 16$ for $k = 1 \text{ Mpc}^{-1}$ to $z \sim 15$ for $k = 0.1 \text{ Mpc}^{-1}$. The peak also becomes much more pronounced at the larger scales, which matches the typical 21-cm fluctuations scale due to inhomogeneous heating (on the order of tens of Mpc). In absence of X-rays, the evolution is markedly different on all scales. At large k , the 21-cm fluctuations only increase: initially gently due to the rising density fluctuations from structure formation, and later faster due to the increased ionization patchiness and its contrast with the cold IGM. At larger scales, the small ionized patches do not contribute, resulting in an initial dip and subsequent rise in the power. Both of these features more pronounced at the larger scales. In the high- T_K limit, the fluctuations are much lower and mostly flat at all scales due to the lack of cold IGM, which results in lower amplitude signal driven initially by the density fluctuations and later by the ionization ones. The evolution of the $k = 0.1 \text{ Mpc}^{-1}$ mode is roughly in agreement with the semi-numerical results of (Mesinger et al. 2013) for the period of X-ray heating, with a clear X-ray peak in the fluctuations at that scale. However, their peak is somewhat lower, reaching only about 20 mK (regardless of the model used), while our fluctuations are about 25 per cent higher. Their peak is also reached somewhat earlier, again likely due to the higher assumed efficiency of their sources, as discussed previously. Other analytical and semi-numerical models, such as Pritchard & Furlanetto (2007) and Santos et al. (2010) find a similar lower peak value for that mode, again of order 20 mK; while Fialkov et al. (2014) find an even lower peak value, below 20 mK. The reasons for this are not clear, but these approximate models (from several different codes) appear to systematically find lower fluctuations than our result.

In Fig. 7, we show maps of the mean-subtracted differential brightness temperature ($\delta T_b - \overline{\delta T_b}$) at several key epochs of the

redshifted 21-cm evolution, smoothed with a Gaussian beam that is roughly twice as broad as the what can be achieved by the core of SKA1-Low, which will have maximum baselines of around 2 km. We also averaged over a frequency bandwidth which corresponds to the same spatial scale as the Gaussian beam. To mimic the lack of sensitivity at large scales, which interferometers have due to the existence of a minimum distance between their elements, we also subtracted the mean value from the images. We do not include instrument noise and calibration effects in these maps. However, at this resolution, SKA1-Low is expected to have a noise level of $\sim 10 \text{ mK}$ per resolution element for 1000 hours of integration (Koopmans et al. 2015).

The images show a clear difference between the cases with and without X-ray heating even at these low resolutions, suggesting that SKA should be able to distinguish between these two scenarios. As the variations over the FoV reach values of 50 mK we can also conclude that SKA1-Low will be able to image these structures for deep integrations of around 1000 hours. Previous expectations were that SKA1-Low would only be able to make statistical detections of the 21cm signal from the Cosmic Dawn. Our results indicate that, at least from the perspective of signal to noise, imaging should be possible.

Once again, the signal from partially heated IGM peaks around $z \sim 16$, when there are large regions – tens of Mpc across – in either emission or absorption. This peak is followed by gradual thorough heating of the IGM above T_{CMB} , bringing the signal all in emission and, thus, decreasing the overall fluctuations. In the stellar-only case, the maps remain fully in absorption at these resolutions, since the heated regions are much smaller than the beam extent and are smoothed away. Nonetheless, considerable fluctuations remain, with high overall amplitude due to the very cold IGM in that case. By the time some larger regions are substantially affected by ionization, the contrast in the images becomes large ($z \sim 13$).

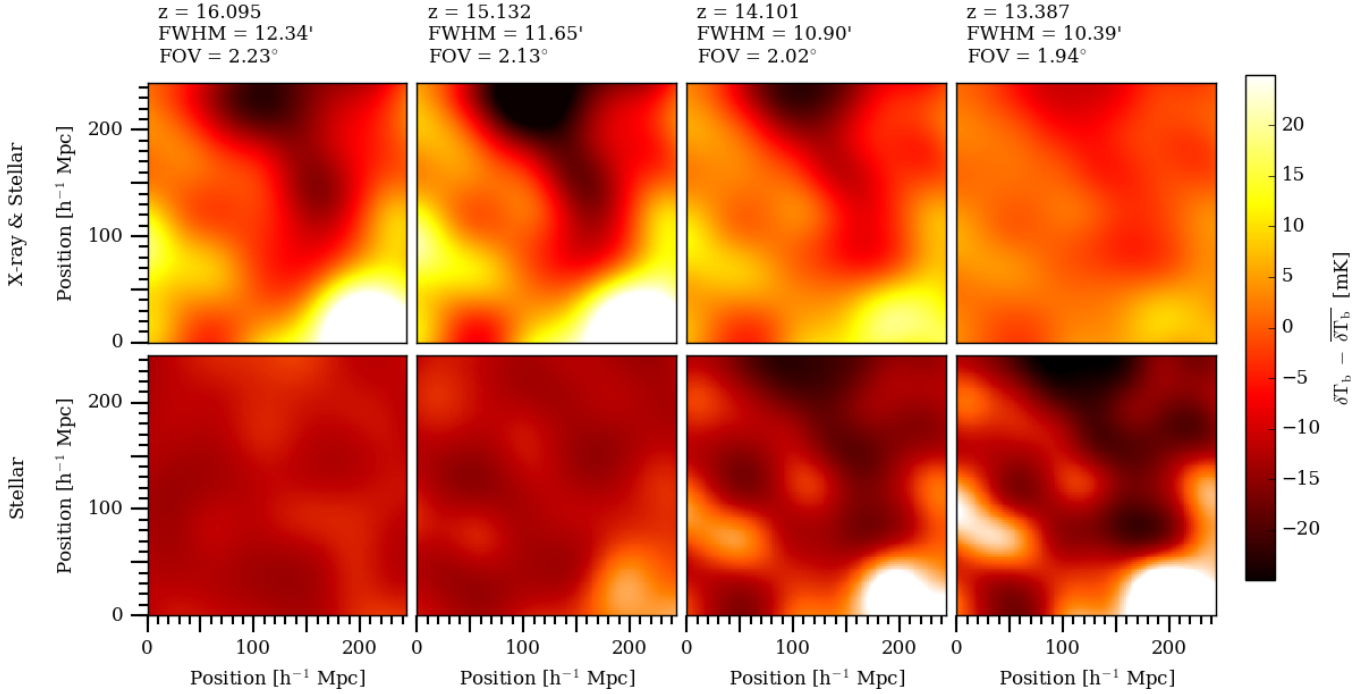


Figure 7. Mean-subtracted differential brightness temperature maps smoothed with a Gaussian beam with the full-width half-maximum (FWHM) corresponding to a 1.2 km maximum baseline at the relevant frequency, as labelled. The images are bandwidth-smoothed with a top hat function (width equal to the distance corresponding to the beam width). The X-ray simulation runs along the top row and the stellar only case is below, with snapshots of the same redshifts being vertically aligned.

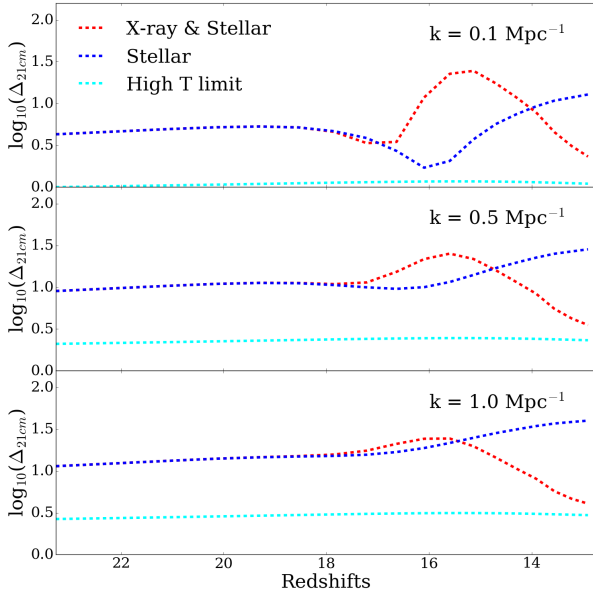


Figure 6. The evolution of the 21-cm power spectra modes at $k = 0.1, 0.5$ and 1 Mpc^{-1} for the two simulations and high- T_K limit for reference, as labelled.

4.3 21-cm ONE-POINT STATISTICS

The 21-cm fluctuations are typically non-Gaussian in nature and are not fully described by the power spectra alone, though imaging might not be possible in all regimes for sensitivity reasons. Therefore, the one-point statistical properties of the 21-cm signal are also

of great interest, since they quantify other aspects of the 21-cm signal and enable comparisons with past works and future observations. We use the dimensionless definitions for rms, skewness, and kurtosis, as follows:

$$\text{rms}(y) \equiv \sigma = \sqrt{\frac{\sum_{i=0}^N (y_i - \bar{y})^2}{N}}, \quad (8)$$

$$\text{Skewness}(y) = \frac{1}{N} \frac{\sum_{i=0}^N (y_i - \bar{y})^3}{\sigma^3}, \quad (9)$$

and

$$\text{Kurtosis}(y) = \frac{1}{N} \frac{\sum_{i=0}^N (y_i - \bar{y})^4}{\sigma^4}. \quad (10)$$

Here, y is the quantity of interest (in this case δT_b), N is the number of data points, \bar{y} is the mean value of y , and σ^2 is the variance of y . These quantities are calculated from coeval simulation cubes, smoothed with a Gaussian beam corresponding to a 1.2 km maximum baseline at the relevant frequency and a bandwidth corresponding to the same spatial extent as the FWHM of the beam. This is the same smoothing as was used for the images in Fig. 7.

In the top left panel of Fig. 8, we show the global value of the differential brightness temperature, $\overline{\delta T_b}$, calculated as the mean signal from our simulations, along with the high- T_K limit case. The global value starts negative, due to the initially cold IGM, and drops further as the universe expands and cools adiabatically. In the stellar-only case, $\overline{\delta T_b}$ rises slowly thereafter, starting at $z \sim 16.5$ as the highest density peaks become ionized. The highest value remains negative, since the neutral IGM never gets heated in this scenario. $\overline{\delta T_b}$ is significantly higher in the X-ray & stellar case, starting from around $z = 20$ due to heating of the IGM. The

global value becomes positive just before $z = 14$ after which and it asymptotically approaches the high- T_K limit. The evolution of the global 21cm signal is similar to that of the analytical and semi-numerical models in the literature, (e.g. Pritchard & Furlanetto 2007; Mesinger et al. 2013), apart from the timing of this transition, which depends on the specific assumptions made about the ionizing and X-ray sources. One difference from these models is that we do not model the early Ly α background, but assume efficient WF coupling at all times. When this assumption is not made, weaker WF coupling early on produces a less deep absorption signal (typically $\delta T_{b,\min} > 180$ mK instead of $\delta T_{b,\min} \sim 200$ mK as in our case). While the incomplete Ly α coupling could be an important effect at the earliest times ($z > 20$), we focus on the subsequent X-ray heating epoch, where this effect should have minimal impact.

The lower lefthand panel of Fig. 8 shows the rms or standard deviation of the differential brightness temperature as a function of redshift, calculated according to Eq. 8 and for the resolution specified below Eq. 10. Before the X-ray heating is able to have significant impact on the cold IGM, our two scenarios have a similar rms evolution, which is dominated by the density fluctuations and the adiabatic cooling of the IGM. Later on, the rms drops slightly in both cases due to the ionization of the high density peaks around the first ionizing sources, combined with local X-ray heating in the X-rays and the high energy photons from the stellar radiation model which brings the local IGM temperature closer to the CMB. Both heating and local ionization introduce small-scale δT_b fluctuations, which are smoothed out by the beam and bandwidth averaging. As the characteristic scale of the X-ray heating fluctuations increases (cf. the power spectra evolution), the rms starts rising again and peaks at ~ 18 mK around $z \sim 15$. Thereafter, the rms fluctuations gradually decrease due to the mean differential brightness temperature rising towards positive values and 21-cm absorption turning into emission.

At later times, the rms in the case with X-ray heating asymptotically approaches the high- T_K limit, but does not quite reach it by the end of the simulation at $z = 12.7$. In the stellar-only case, the rms of δT_b is driven purely by the density and ionization fluctuations. The rms, therefore, initially decreases more slowly than the X-ray & stellar case, reaches a minimum around $z \sim 16$, then strongly increases until the end of the simulation due to the large contrast between the (ever larger) ionized regions and extended, cold absorption regions. The features of the rms evolution and their timing are dependent on the resolution available and, hence, on the details of the radio interferometer.

The higher order statistics of δT_b are also affected by the inclusion of X-rays. The skewness of δT_b is shown in the top right panel of Fig. 8. In both cases, the skewness starts close to zero as it tracks the initial, Gaussian density fields. The skewness then gradually increases in both cases as hot regions surrounding sources positively skew the data. The skewness from the X-ray & stellar case then increases more rapidly than that of the stellar-only case, as large regions of the IGM are heated. The skewness for the X-ray & stellar case peaks around $z \sim 17$ with a value of 1.20. After this peak, the skewness decreases as the heating becomes more homogeneous and becomes negative before increasing and approaching the high- T_K limit (shown in yellow). The skewness from the stellar-only case follows a similar pattern, peaking at a later time $z \sim 14.7$ and a higher value of 1.27, before decreasing. Once again, the high- T_K limit is not valid for the skewness at the early times considered in this work, except for the very last stages of the X-ray & stellar case. Our skewness results are in reasonable agreement with

the ones for low X-ray efficiency case “log $\zeta_X = 55$ ” in Watkinson & Pritchard (2015) (cf. their Fig. 13, but note that they show the dimensional skewness, which is the same as the dimensionless skewness multiplied by the corresponding rms).

The kurtosis of δT_b from our two simulations is displayed in the bottom right panel of Fig. 8. Initially, the kurtosis of both models is close to zero as the Gaussian density fluctuations dominate at these early stages. As long-range heating develops, the kurtosis of the X-ray & stellar case increases and peaks at $z \sim 17.2$ with a value of 2.8. Later, the kurtosis decreases again to negative values before increasing once more and approaching temperature saturation (plotted in yellow). This statistic follows roughly the same pattern as the skewness, but with somewhat different functional shape and timing. The stellar-only case kurtosis follows a comparable pattern, peaking at $z \sim 15.36$ with a value of 3.3, and then decreasing to very low values towards the end of the simulation.

5 CONCLUSIONS

We presented the first large-volume, fully numerical structure formation and radiative transfer simulations of the IGM heating during the Cosmic Dawn by the first stellar and X-ray sources and the resultant the 21-cm signals from this epoch. We simulate the multi-frequency transfer of both ionizing and X-ray photons and solve self-consistently for the temperature state of the IGM. While the exact nature and properties of the first X-ray sources are still quite uncertain, our results demonstrate that, under a reasonable set of assumptions, these sources produce significant early and inhomogeneous heating of the neutral IGM and, thus, impact considerably the redshifted 21-cm signals.

In this work, we considered relatively soft-spectrum X-ray sources, which trace the star formation at high redshift. At these high redshifts, these sources are still fairly rare and for reasonable assumed efficiencies, the addition of X-rays does not affect significantly the evolution of the mean fractions of singly ionized H and He. The fraction of He III is more significantly affected, however, boosted by almost an order of magnitude compared to the stellar-only case; although it nevertheless remains quite low overall.

In contrast, the high energies and long mean free paths of the hard X-ray radiation make it the dominant driver of the heating of the neutral IGM. Pop. II stars, even massive ones, do not produce a significant amount of such hard radiation. Therefore, both the morphology and the overall amount of heating change dramatically when X-ray sources are present. The mean and the median temperature both increase considerably compared to the stellar-only case, with the mean eventually reaching $\sim 10^3$ K by $z \sim 13$ (the median, which only reaches ~ 200 K, better reflects the neutral IGM state as it is less sensitive to the very high temperatures in the ionized regions). The X-ray heating is long-range and therefore widely distributed throughout the IGM. This heating is also highly inhomogeneous, as evidenced by the temperature PDFs, maps and evolution seen in the lightcone visualizations. The neutral regions are heated by the X-ray sources and go fully into 21-cm emission with respect to the CMB before $z = 13$, while with stellar-only sources the IGM remains in absorption throughout the Cosmic Dawn. The presence of X-rays, therefore, results in an early, but extended ($\Delta z \sim 7$) transition into emission.

The 21-cm fluctuations initially ($z > 18$) track the density fluctuations due to the still insignificant heating and ionization fluctuations. However, the temperature fluctuations due to X-ray heating quickly boost the large-scale 21-cm fluctuations to much higher

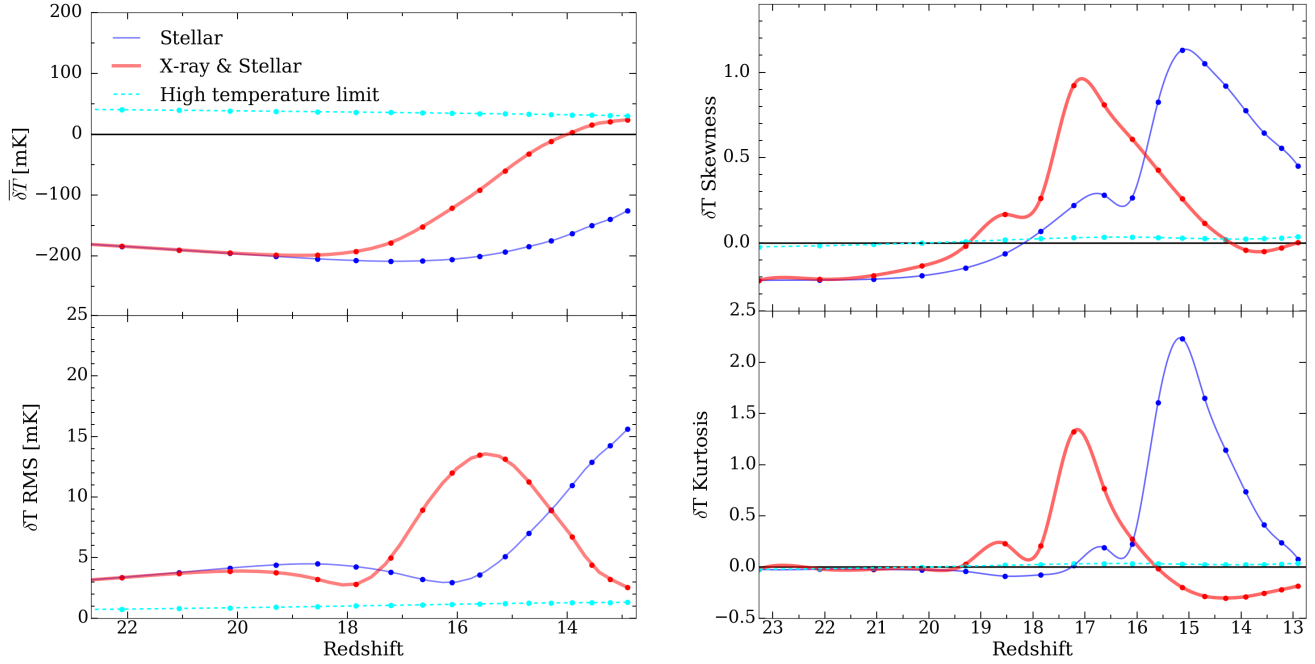


Figure 8. Statistics from the 21-cm signal from both our simulations as well as the high- T_K limit. The top left panel shows the mean value of δT_b , the bottom left panel the rms, the top right panel the skewness and the bottom right the kurtosis. The points are the results calculated from smoothed coeval boxes from our simulations and the fitted line is a cubic spline of these data.

values. At a resolution of $\sim 10 - 12$ arcmin for redshifts $14 - 16$, the fluctuations are large enough to be several factors above the expected noise level of SKA1-Low, which implies the possibility of observing not only power spectra, but also coarse images of the 21-cm signal from the Cosmic Dawn. For the same resolution the differential brightness temperature rms in presence of X-rays peaks at ~ 18 mK around $z \sim 15$. The temperature fluctuations also create a characteristic low- k peak of the 21-cm power spectra, which is initially at $k \sim 0.3 - 1 \, h \, \text{Mpc}^{-1}$, but quickly moves to larger scales at $k \sim 0.2 \, h \, \text{Mpc}^{-1}$ (corresponding to spatial scale of about 30 Mpc) at $z \sim 14 - 15$. In contrast, the stellar-only case fluctuations are still increasing steeply by $z \sim 12$ due to the extensive cold patches remaining. As the IGM heats up and the absorption gradually turns into emission, the 21-cm fluctuations for X-rays & stellar radiation decrease and asymptote to the high- T_K limit, which is not fully reached by the end of our simulation ($z \sim 12.7$), even though by that time the mean IGM is heated well above the CMB temperature.

The distribution of the differential brightness temperature fluctuations shows a clear non-Gaussian signature, with both the skewness and kurtosis positive and peaking just when the fluctuations start rising. In both simulations, the signal goes back to Gaussian. In the presence of X-ray heating, the 21-cm signal returns to Gaussian faster, within $\Delta z \sim 4$ for skewness and $\Delta z \sim 2$ for kurtosis. While for soft radiation sources, the non-Gaussianity peak is relatively more extended.

The often-used high spin temperature limit, $T_S \gg T_{\text{CMB}}$, is not valid during the X-ray heating epoch as long as any IGM patches remain cold. When X-rays are present, even after the IGM temperature rises above the CMB everywhere (and thus the 21-cm signal transits into emission), significant temperature fluctuations remain and contribute to the 21-cm signal. The neutral regions do not asymptote to the high-temperature limit until quite late in our

model, at $z \sim 12$. This asymptotic behaviour can readily be seen in the power spectra and statistics of the 21-cm signal. Soft, stellar-only radiation has short mean free paths and, thus, never penetrates into the neutral regions, leaving cold neutral patches.

Previous work in this area has largely been limited to approximate semi-analytical and semi-numerical modelling (e.g. Pritchard & Furlanetto 2007; Mesinger et al. 2013; Fialkov & Barkana 2014; Shimabukuro et al. 2015; Watkinson & Pritchard 2015; Kubota et al. 2016). By their nature, such approaches do not apply detailed, multi-frequency RT, but rely on counting the photons produced in a certain region of space and compares this to the number of atoms (with some correction for the recombinations occurring). The difference between the two determines the ionization state of that region. The X-ray heating is done by solving the energy equation using integrated, average optical depths and photon fluxes, and often additional approximations are employed as well (e.g. Watkinson & Pritchard 2015). These methods typically do not take into account nonlinear physics, spatially varying gas clumping or absorbers, or Jeans mass filtering of low mass sources. These differences make comparisons with the previous results in detail difficult due to the very different modelling employed and would require further study. Nonetheless, we find some commonalities and some disparities with our results, summarised below.

Our thermal history is similar to that of the relevant cases in Pritchard & Furlanetto (2007) (their Case A) and Watkinson & Pritchard (2015) (their case “ $\log \zeta_X = 55$ ”). We find a quite extended transition between 21-cm absorption and emission, from the formation of the first ionizing and X-ray sources at $z \sim 21$ all the way to $z \sim 13$. This transition is somewhat more protracted than the one in the most similar scenarios ($f_X = 1$ and 5) considered in Mesinger et al. (2013), likely due to the higher star formation efficiencies assumed in that work.

We find a clear X-ray heating-driven peak in the 21-cm power

spectra at $k = 0.2 - 0.3 h \text{ Mpc}^{-1}$, similar to the soft X-ray spectra peak found in Pacucci et al. (2014) and at similar redshift ($z \sim 15 - 16$; though this depends on the uncertain source efficiencies). Their peak power, at $\Delta_{21\text{cm}} \sim 15 \text{ mK}$ is appreciably lower than what we find, $\Delta_{21\text{cm}} \sim 25 \text{ mK}$. The same is true for the power spectra evolution found in Pritchard & Furlanetto (2007). While the general evolution appears similar, with the fluctuations at $k = 0.1 \text{ Mpc}^{-1}$ also peaking at $z \sim 15 - 16$ (although $z \sim 12 - 13$ for the scenario with less X-rays, again suggesting a strong dependence on the source model), the power found is much lower than our results. This difference is particularly pronounced on smaller scales, with peak values of $\Delta_{21\text{cm}} \sim 19 \text{ mK}$ or $\Delta_{21\text{cm}} \sim 11 \text{ mK}$ depending on the source model used by them, compared to $\Delta_{21\text{cm}} \sim 32 \text{ mK}$ for our X-ray & stellar radiation case. Overall, the peak power spectra values derived from analytical and semi-numerical models appear systematically lower than our results. The reasons for this peak amplitude difference will have to be investigated in future work.

The 21-cm skewness from the X-ray heating epoch is rarely calculated, but Watkinson & Pritchard (2015) recently found a very similar evolution to ours (though shifted to somewhat higher redshifts), with a positive peak roughly coinciding with the initial rise of the 21-cm fluctuations due to the temperature patchiness. Their corresponding 21-cm differential brightness temperature PDF distributions during the X-ray heating epoch significantly differ from ours, however. At the epoch when T_S reaches a minimum the semi-numerical model predicts a long tail of positive differential brightness temperature, which does not exist in the full simulations. Around the $T_S \sim T_{\text{CMB}}$ epoch, our distribution is quite Gaussian; while Watkinson & Pritchard (2015) find an asymmetric one (though, curiously, with one with close to zero skewness, indicating that skewness alone provides a very incomplete description). Finally, in the $T_S \gg T_{\text{CMB}}$ epoch, the two results both yield gaussian PDFs, but the simulated one is much narrower.

Our models confirm that, for reasonable assumptions about the presence of X-ray sources, there is a period of substantial of fluctuations in the 21-cm signal caused by the patchiness of this heating and that this period precedes the one in which fluctuations are mostly caused by patchiness in the ionization. However, since the nature and properties of X-ray sources remain unconstrained by observations, other scenarios in which the heating occurs later, are also allowed. The currently ongoing observational campaigns of both LOFAR and MWA should be able to put constraints on the presence of spin temperature fluctuations for the range $z < 11$, which would then have clear implications for the required efficiency of X-ray heating at those and earlier redshifts. In the future, we will use simulations of the kind presented here to explore other possible scenarios, for example heating caused by rare, bright sources, as well as the impact of spin temperature fluctuations on all aspects of the 21-cm signal, such as redshift space distortions.

6 ACKNOWLEDGEMENTS

This work was supported by the Science and Technology Facilities Council [grant number ST/I000976/1] and the Southeast Physics Network (SEPNet). GM is supported in part by Swedish Research Council grant 2012-4144. This research was supported in part by the Munich Institute for Astro- and Particle Physics (MIAPP) of the DFG cluster of excellence “Origin and Structure of the Universe”. We acknowledge that the results in this paper have been achieved using the PRACE Research Infrastructure resource Marenostrum

based in the Barcelona Supercomputing Center, Spain. Some of the numerical computations were done on the Apollo cluster at The University of Sussex.

REFERENCES

- Ahn K., Iliev I. T., Shapiro P. R., Srisawat C., 2015a, MNRAS, 450, 1486
Ahn K., Xu H., Norman M. L., Alvarez M. A., Wise J. H., 2015b, ApJ, 802, 8
Baek S., Semelin B., Di Matteo P., Revaz Y., Combes F., 2010, Astron. & Astrophys., 523
Bolton J. S., Becker G. D., Raskutti S., Wyithe J. S. B., Haehnelt M. G., Sargent W. L. W., 2012, MNRAS, 419, 2880
Ciardi B., Madau P., 2003, ApJ, 596, 1
Crocce M., Puelblas S., Scoccimarro R., 2006, MNRAS, 373, 369
Dixon K. L., Iliev I. T., Mellema G., Ahn K., Shapiro P. R., 2016, MNRAS, 456, 3011
Fan X., Strauss M. A., Becker R. H., White R. L., Gunn J. E., Knapp G. R., Richards G. T., Schneider D. P., Brinkmann J., Fukugita M., 2006, AJ, 132, 117
Fialkov A., Barkana R., 2014, MNRAS, 445, 213
Fialkov A., Barkana R., Visbal E., 2014, Nature, 506, 197
Field G. B., 1958, Proceedings of the IRE, 46, 240
Friedrich M. M., Mellema G., Iliev I. T., Shapiro P. R., 2012, MNRAS, 421, 2232
Furlanetto S. R., Hernquist L., Zaldarriaga M., 2004, MNRAS, 354, 695
Glover S. C. O., Brand P. W. J. L., 2003, MNRAS, 340, 210
Greiner J., Krühler T., Fynbo J. P. U., Rossi A., Schwarz R., Klose S., Savaglio S., Tanvir N. R., McBreen S., Totani T., Zhang B. B., Wu X. F., Watson D., Barthelmy S. D., Beardmore A. P., Ferrero P., Gehrels N., Kann D. A., Kawai N., Yoldaş A. K., Mészáros P., Milvang-Jensen B., Oates S. R., Pierini D., Schady P., Toma K., Vreeswijk P. M., Yoldaş A., Zhang B., Afonso P., Aoki K., Burrows D. N., Clemens C., Filgas R., Haiman Z., Hartmann D. H., Hasinger G., Hjorth J., Jehin E., Levan A. J., Liang E. W., Malesani D., Pyo T.-S., Schulze S., Szokoly G., Terada K., Wiersema K., 2009, ApJ, 693, 1610
Haiman Z., Holder G. P., 2003, ApJ, 595, 1
Harnois-Déraps J., Pen U.-L., Iliev I. T., Merz H., Emberson J. D., Desjacques V., 2013, MNRAS, 436, 540
Iliev I. T., Ciardi B., Alvarez M. A., Maselli A., Ferrara A., Gnedin N. Y., Mellema G., Nakamoto T., Norman M. L., Razoumov A. O., Rijkhorst E.-J., Ritzerveld J., Shapiro P. R., Susa H., Umemura M., Whalen D. J., 2006, MNRAS, 371, 1057
Iliev I. T., Mellema G., Ahn K., Shapiro P. R., Mao Y., Pen U.-L., 2014, MNRAS, 439, 725
Iliev I. T., Mellema G., Shapiro P. R., Pen U.-L., 2007, MNRAS, 376, 534
Iliev I. T., Mellema G., Shapiro P. R., Pen U.-L., Mao Y., Koda J., Ahn K., 2012, MNRAS, 423, 2222
Iliev I. T., Whalen D., Mellema G., Ahn K., Baek S., Gnedin N. Y., Kravtsov A. V., Norman M., Raicevic M., Reynolds D. R., Sato D., Shapiro P. R., Semelin B., Smidt J., Susa H., Theuns T., Umemura M., 2010, MNRAS, 400, 1283
Khaire V., Srianand R., Choudhury T. R., Gaikwad P., 2016, MNRAS, 457, 4051
Kneivitt G., Wynn G. A., Power C., Bolton J. S., 2014, MNRAS, 445, 2034
Komatsu E., Smith K. M., Dunkley J., Bennett C. L., Gold B.,

- Hinshaw G., Jarosik N., Larson D., Nolte M. R., Page L., Spergel D. N., Halpern M., Hill R. S., Kogut A., Limon M., Meyer S. S., Odegard N., Tucker G. S., Weiland J. L., Wollack E., Wright E. L., 2011, *ApJS*, 192, 18
- Koopmans L., Pritchard J., Mellema G., Aguirre J., Ahn K., Barkana R., van Bemmelen I., Bernardi G., Bonaldi A., Briggs F., de Bruyn A. G., Chang T. C., Chapman E., Chen X., Ciardi B., Dayal P., Ferrara A., Fialkov A., Fiore F., Ichiki K., Iliev I. T., Inoue S., Jelic V., Jones M., Lazio J., Maio U., Majumdar S., Mack K. J., Mesinger A., Morales M. F., Parsons A., Pen U. L., Santos M., Schneider R., Semelin B., de Souza R. S., Subrahmanyam R., Takeuchi T., Vedantham H., Wagg J., Webster R., Wyithe S., Datta K. K., Trott C., 2015, *Advancing Astrophysics with the Square Kilometre Array (AASKA14)*, 1
- Kubota K., Yoshiura S., Shimabukuro H., Takahashi K., 2016, *ArXiv e-prints* 1602.02873
- Lee K.-Y., Mellema G., Lundqvist P., 2016, *MNRAS*, 455, 4406
- Lewis A., Challinor A., Lasenby A., 2000, *ApJ*, 538, 473
- Lutovinov A., Revnivtsev M., Gilfanov M., Shtykovskiy P., Molkov S., Sunyaev R., 2005, *A&A*, 444, 821
- McGreer I. D., Mesinger A., D’Odorico V., 2015, *MNRAS*, 447, 499
- Mellema G., Iliev I. T., Alvarez M. A., Shapiro P. R., 2006, *Elsevier Science*, 11, 374
- Mesinger A., Ferrara A., Spiegel D. S., 2013, *MNRAS*, 431, 621
- Mineo S., Gilfanov M., Sunyaev R., 2012, *MNRAS*, 419, 2095
- Pacucci F., Mesinger A., Mineo S., Ferrara A., 2014, *MNRAS*, 443, 678
- Pentericci L., Vanzella E., Fontana A., Castellano M., Treu T., Mesinger A., Dijkstra M., Grazian A., Bradač M., Conselice C., Cristiani S., Dunlop J., Galametz A., Giavalisco M., Giallongo E., Koekemoer A., McLure R., Maiolino R., Paris D., Santini P., 2014, *ApJ*, 793, 113
- Planck Collaboration, Adam R., Aghanim N., Ashdown M., Aumont J., et al B., 2016, *ArXiv e-prints* 1605.03507
- Planck Collaboration, Ade P. A. R., Aghanim N., Arnaud M., Ashdown M., Aumont J., Baccigalupi C., Banday A. J., Barreiro R. B., Bartlett J. G., et al., 2015, *ArXiv e-prints* 1502.01589
- Pritchard J. R., Furlanetto S. R., 2007, *MNRAS*, 376, 1680
- Pritchard J. R., Loeb A., 2012, *Reports on Progress in Physics*, 75, 086901
- Raga A. C., Mellema G., Arthur S. J., Binette L., Ferruit P., Steffen W., 1999, *Revista Mexicana de Astronomia y Astrofisica*, 35, 123
- Raskutti S., Bolton J. S., Wyithe J. S. B., Becker G. D., 2012, *MNRAS*, 421, 1969
- Santos M. G., Ferramacho L., Silva M. B., Amblard A., Cooray A., 2010, *MNRAS*, 406, 2421
- Schenker M. A., Stark D. P., Ellis R. S., Robertson B. E., Dunlop J. S., McLure R. J., Kneib J.-P., Richard J., 2012, *ApJ*, 744, 179
- Shimabukuro H., Yoshiura S., Takahashi K., Yokoyama S., Ichiki K., 2015, *MNRAS*, 451, 467
- Stark D. P., Ellis R. S., Ouchi M., 2011, *ApJL*, 728, L2
- Theuns T., Bernardi M., Frieman J., Hewett P., Schaye J., Sheth R. K., Subbarao M., 2002, *ApJL*, 574, L111
- Tilvi V., Papovich C., Finkelstein S. L., Long J., Song M., Dickinson M., Ferguson H. C., Koekemoer A. M., Giavalisco M., Mobasher B., 2014, *ApJ*, 794, 5
- Totani T., Kawai N., Kosugi G., Aoki K., Yamada T., Iye M., Ohta K., Hattori T., 2006, in *IAU Joint Discussion*, Vol. 7, IAU Joint Discussion
- Watkinson C. A., Pritchard J. R., 2015, *MNRAS*, 454, 1416
- Xu H., Ahn K., Wise J. H., Norman M. L., O’Shea B. W., 2014, *ApJ*, 791, 110